Experimental and numerical investigation of ductile fracture for AA6061-T6 sheets at room and elevated temperatures

Ahmed Kacem, Hervé Laurent, Sandrine Thuillier

Experimental and numerical investigation of ductile fracture for AA6061-T6 sheets at room and elevated temperatures

Ahmed Kacem[a,*], Hervé Laurent[a], Sandrine Thuillier[a]

[a] *Univ. Bretagne Sud, UMR CNRS 6027, IRDL, F-56100 Lorient, France*

Abstract

Warm forming is largely employed to enhance the poor formability of aluminum alloys at room temperature. The knowledge of the effect of stress state and temperature on the forming limits is an important aspect for the control of warm forming operations. Therefore, the objective of this work is to investigate the influence of temperature on the ductile fracture of AA6061-T6 aluminum alloy sheet metal under different stress states, ranging from shear to biaxial tension. For this purpose, experiments and numerical simulations of uniaxial tensile tests on dog-bone shaped specimen, notched specimens with different radius, specimens with a central hole and shear specimens are conducted at room and elevated temperatures. The hybrid experimental-numerical approach is used to identify the fracture strain and the corresponding stress state parameters (i.e. stress triaxiality and Lode parameter) to derive the fracture loci at room temperature, 150 °C and 200 °C. To accurately model the material behavior, the positive strain rate sensitivity in the flow stress response at elevated temperature is considered and attention is paid to constrain the finite element model by using the real experimental

*Corresponding author

boundary conditions. A strong dependency of the ductile fracture on the temperature and stress state is evidenced. Also, an extension of Lou's ductile fracture criterion which includes the impact of temperature on ductile fracture prediction is proposed. The prediction accuracy of the original and extended criteria is evaluated. It is found that Lou's ductile fracture criterion is well suited to predict accurately ductile fracture at elevated temperatures under isothermal conditions whereas the extended form is very useful to predict ductile fracture initiation under non-isothermal conditions.

Keywords: Temperature, AA6061-T6, Ductile fracture, Stress state

1. Introduction

Aluminum alloys are extensively used in the metal forming industry due to their high strength to weight ratio and excellent corrosion resistance. However, their poor formability at room temperature limits their use and makes them less attractive than steel. Warm forming is increasingly used to enhance the failure limits and therefore to manufacture complex structural components made from aluminum alloys. Moreover, the large variety of stress states encountered during a forming process must be taken into account. Indeed, it is now well known that the forming limits depend strongly on the stress state which may be described by the stress triaxiality η and the Lode parameter L defined by:

$$\eta = \frac{\sigma_m}{\bar{\sigma}} \qquad \text{with} \qquad \sigma_m = \frac{\sigma_1 + \sigma_2 + \sigma_3}{3} \tag{1}$$

$$L = \frac{2\sigma_2 - \sigma_1 - \sigma_3}{\sigma_1 - \sigma_3} \tag{2}$$

where σ_m is the hydrostatic stress, $\bar{\sigma}$ is von Mises equivalent stress and σ_1, σ_2 and σ_3 are the principal stresses of the stress tensor, such that $\sigma_1 \geq \sigma_2 \geq \sigma_3$.

Hancock and Mackenzie [1] found out that the formability depends markedly on the stress triaxiality via a series of tests carried out on circumferentially notched tensile specimens. Mirza et al. [2] investigated the effect of stress triaxiality on the fracture characteristics of ductile metals for high stress triaxiality level. It was evidenced that the ductility of all tested materials is strongly dependent on the stress triaxiality, this dependency being higher for the ferrous materials than for aluminium alloys. Bao and Wierzbicki [3] investigated the dependence of ductile fracture on the stress triaxiality in a wide range of this parameter by a series of tests including upsetting tests, shear tests and tensile tests on AA2024-T351 aluminum alloy, showing the strong dependency between formability and stress triaxiality. Zhang et al. [4] claimed that besides stress triaxiality, the Lode parameter should be considered to give a complete description of the stress state. Wierzbicki et al. [5] and Gao and Kim [6] observed that predictions of ductile failure can be improved by introducing the Lode parameter.

Forming limits are not only related to the stress state, but also depend on temperature and strain rate. Shehata et al. [7] investigated the formability of aluminum-magnesium alloys at temperatures ranging from 20 °C to 300 °C, for several strain rates in both uniaxial and biaxial tension, by measuring the total elongation in tensile testing and the maximum cup height in punch stretching tests. They found out that, in the biaxial tension defor-

mation mode, the material is less sensitive to temperature and strain rate than in uniaxial tension. Ayres and Wenner [8] investigated the forming limits of AA5182-O by performing tensile and cup tests up to failure at 25 °C, 130 °C and 200 °C at different strain rates. It was concluded that the limit strains increase at elevated temperature leading to higher forming limit diagrams. Clausen et al [9] showed a considerable increase in the fracture strain of AA5083–H116 at 400 °C, compared to room temperature. Li and Ghosh [10] performed biaxial warm forming test for three automotive aluminum sheet alloys, namely AA5757, AA5182 and AA6111-T4, in the temperature range 200-350 °C. It was found out that all tested alloys exhibit a significant improvement of their formability and the magnitude of this effect depends on the aluminum grade. Mahabunphachai and Koç [11] evidenced through tensile and bulge tests that the formability of AA5052 and AA6061 sheets increases with temperature and decreases with strain rate. Similar observations are made by Chu et al. [12] for AA5086 using a Marciniak test setup. Aditionally, Wang et al. [13] showed that temperature and punch speed have a significant effect on the formability through a cup punch test. They also showed that the forming limits of AA2024 could be improved considerably by forming in the vicinity, but not in excess, of 450 °C. Recently, Kacem et al. [14] showed a strong dependency of the ductile fracture of AA6061 sheets on the temperature and stress state.

Ductile Fracture (DF) criteria are widely used to assess the metal formability limits. The prediction of ductile fracture can be achieved by either an uncoupled fracture criterion or a coupled damage model. Simplicity and a reduced number of model parameters to be calibrated are the main advan-

tages of the uncoupled ductile fracture criteria, making them very attractive for industrial applications. In such an approach, the onset of fracture is predicted when the integral of plastic deformation, multiplied by a weighting function depending on the stress state, reaches a critical value. By using different weighting functions, several DF criteria based on this approach have been proposed in the literature at room temperature as shown in Tab.1.

DF criterion	Formulation
Rice and Tracey	$D\left(\bar{\varepsilon}_p\right) = \frac{1}{C_R}\int_0^{\bar{\varepsilon}_f} exp\left(\frac{3}{2}\eta\right) d\bar{\varepsilon}_p$
Ayada	$D\left(\bar{\varepsilon}_p\right) = \frac{1}{C_A}\int_0^{\bar{\varepsilon}_f} \eta \, d\bar{\varepsilon}_p$
Lou	$D\left(\bar{\varepsilon}_p\right) = \frac{1}{C_3}\int_0^{\bar{\varepsilon}_f} \left(\frac{2}{\sqrt{L^2+3}}\right)^{C_1} \left(\frac{\langle 1+3\eta\rangle}{2}\right)^{C_2} d\bar{\varepsilon}_p$

Table 1: Some typical examples of DF criteria (Rice and Tracey [15], Ayada [16] and Lou [17, 18]). D is a failure indicator that gives the onset of fracture when it reaches unity. $\bar{\varepsilon}_p$ is the equivalent plastic strain. $\bar{\varepsilon}_f$ is the fracture strain. C_R, C_A, C_1, C_2 and C_3 are material parameters.

Rice and Tracey [15], Oyane [19], Ayada et al. [16] and Ko et al. [20] proposed DF criteria that consider only the stress triaxiality effect on the ductile fracture. Bai and Wierzbicki [21, 22] proposed the Modified Mohr-Coulomb (MMC) criterion which considers the effect of both the stress triaxiality and Lode parameter. Mohr and Marcadet [23] developed the Hosford-Coulomb model considering also the effects of the stress triaxiality and the Lode parameter. Lou et al. [17] developed a ductile fracture criterion inspired from the micro-mechanisms of ductile fracture, that occurs mainly due to void nucleation, growth and finally coalescence into microcracks. It was assumed that

void nucleation is proportional to the equivalent plastic strain, void growth is controlled by the stress triaxiality and coalescence of voids is dominated by the shear-linking up of voids governed by the maximum shear stress linked to the Lode parameter.

The ductile fracture depends also on the strain rate and temperature. However, the above-mentioned DF criteria do not consider this dependency making them only suited for isothermal and fixed strain rate conditions. Some ductile fracture criteria are extended to include the effect of temperature and/or strain rate, which makes it possible to account for fracture under non-isothermal and changing strain rate conditions. Novella et al. [24] proposed an extension of Oyane's criterion with the introduction of a function of temperature and strain rate, obtained by a linear interpolation on the basis of the critical damage values obtained in tension for six conditions of temperature and strain rate. This criterion was calibrated by means of tensile tests conducted on smooth specimens only and applied to a cross wedge rolling process carried out on AA6082-T6 bars at elevated temperature. Roth and Mohr [25] extended the Hosford-Coulomb DF criterion by adding the strain rate dependency based on an analogy with the Johnson-Cook criterion [26] to investigate ductile fracture initiation in advanced high strength steel sheets. In a similar way, Liu et al. [27] extended the Bao-Wierzbicki fracture model [3] by adding the strain rate and the temperature dependency to simulate the chip separation in a cutting process of AA2024-T351 cylindrical parts. It was found that the extended model is the most suitable to describe the chip removal behavior of ductile materials. Also in the same manner, Du et al. [28] extended the MMC criterion to investigate the fracture behavior of 3.2 mm

thick AA5383 sheet at high temperatures, spanning from 350 to 450 °C. Wang et al [29] proposed a new DF criterion by adding a temperature-dependent parameter in the MMC criterion, to describe the fracture behavior of AZ31 magnesium alloy sheets as a function of the temperature and stress state. Fracture tests were carried out at room and elevated temperatures using different specimen geometries. However, the fracture strain was measured experimentally on the specimen surface by Digital Image Correlation (DIC) technique, that is not enough to accurately calibrate the fracture criterion since the fracture may initiate within the thickness rather than on the surface in this kind of experiments. More recently, Cao et al. [30] extended Lou's DF criterion [31] by including temperature and strain rate terms in a similar way to Johnson-Cook criterion to study the fracture behavior of AA7075-H112 bulk metal.

Figuring out the relationship between forming limits, temperature, strain rate and stress state is of great importance for providing more understanding of ductile fracture in warm forming conditions. However, from the above-mentioned studies, it is evident that there is still a need for a further investigation of the effect of stress state and temperature on the forming limits of aluminum alloy sheets. The main aim of this work is to study experimentally and numerically the ductile fracture of an aluminum alloy sheet for a wide range of stress states, i.e. from shear to biaxial tensionn at room and elevated temperatures. To this regard Lou's DF criterion is selected to describe the fracture locus and evaluate the forming limits of AA6061-T6 aluminum alloy at room temperature (RT), 150 °C and 200 °C. Indeed, Lou and Huh [32] compared and evaluated the fracture loci constrained by various DF

criteria at room temperature. The comparison demonstrated that the MMC and Lou DF criteria provide the best predictability in a wide range of stress states. Moreover, Lou's DF criterion has been successfully applied for predicting fracture of several aluminum alloys and therefore seems well adapted to predict the onset of fracture in metal forming processes (e.g. AA1050 [33], AA6082-T6 [34] and AA6016-T4 [35]). The ductile fracture criterion is calibrated by the hybrid experimental-numerical approach [36, 37]. To this end, experiments and numerical simulations of uniaxial tensile tests on dog-bone shaped specimen, notched specimens with different radius, specimens with a central hole and shear specimens are conducted at room and elevated temperatures. Since an accurate description of the flow behavior is fundamental in the hybrid approach, the positive strain rate sensitivity at elevated temperature and the initial anisotropy of the sheet are considered. Attention is also paid to accurately constrain the finite element model by using the real experimental boundary conditions measured by DIC. The aim is to determine the fracture strain and the corresponding stress state parameters for each specimen geometry corresponding to a given stress state and temperature. Furthermore, an extension of Lou's DF criterion is suggested to include the effect of temperature on the fracture initiation. The ductile fracture locus obtained by both the original and extended Lou's DF are compared to the experimental results.

2. Material and methods

This section firstly details the material and specimens designed to obtain the different stress states. Then, details of experiments and FE modeling of

ductile fracture tests are described. Finally, DF criterion and the methodology used to calibrate its parameters are presented.

2.1. Material and specimens

AA6061-T6 aluminum alloy, which is widely used for structural components in the automotive industry, is selected for this study.

Five different types of specimens illustrated in Fig.1 are cut from the same 1 mm aluminum sheet using Computer Numerical Control (CNC) waterjet cutting machine. Dog-bone specimen are designed according to ISO 6892-1 standard to conduct monotonic tensile test. Four ductile fracture specimens are chosen in such a way to achieve a wide range of stress states. Notched specimens with small (NR5) and large (NR15) notch radii are considered to achieve a high stress triaxiality [38]. Specimen with a central hole (HR4) is designed to obtain a stress state close to the uniaxial tensile test but with minor necking [36]. Finally, shear specimen (SH) is designed to achieve a low stress triaxiality [39]. Moreover, dog-bone specimens are cut in the rolling direction (RD), as well as in 45 ° and 90 ° to RD, to investigate the anisotropy. Ductile fracture specimens are only extracted along RD. Three samples are prepared for each fracture specimen type and direction.

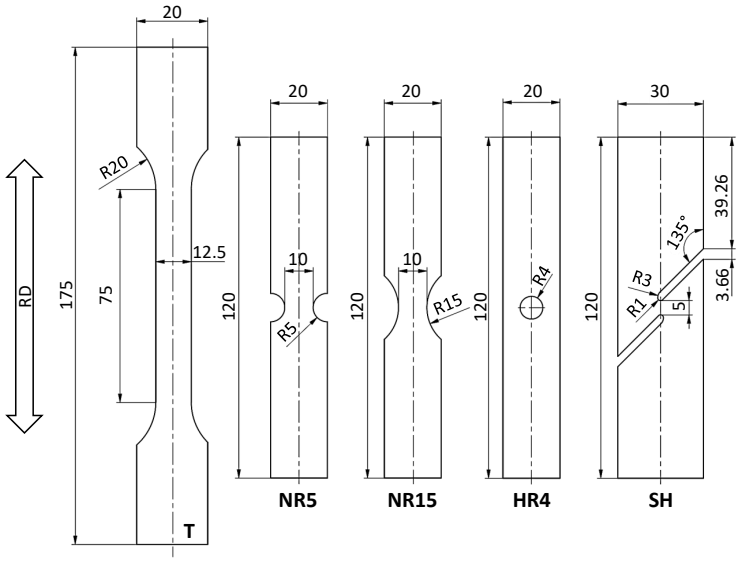

Figure 1: Geometry and dimensions (in mm) of specimens designed to obtain different stress states, (T) dog-bone specimen designed for monotonic tensile test according to ISO 6892-1 standard, (NR5) notched specimen with R = 5 mm, (NR15) notched specimen with R = 15 mm, (HR4) specimen with a central hole with R = 4 mm and (SH) shear specimen. All specimens are extracted from 1 mm AA6061-T6 sheet along RD. Dog-bone specimens are also extracted along 45 ° and 90 ° to RD.

2.2. Tensile and ductile fracture tests

All tests are performed with an INSTRON 5969 universal testing machine equipped with a 50 kN load cell under isothermal conditions (T = RT, 150 °C and 200 °C).

A classical furnace (Matair) is used to heat up the specimen to the testing temperatures of 150 °C and 200 °C. The temperature is measured by two K-type thermocouples attached at the center of the specimen and the grip of the tensile machine respectively. To insure a homogenous temperature on

the specimen during the test, the tensile load is applied when the temperature recorded by both thermocouples reaches the testing temperature within $\pm 2\,^{\circ}\mathrm{C}$. To avoid any thermal stresses due to thermal expansion before applying the tensile load, the load is maintained close to zero by moving the crosshead manually during the heating stage. Two tests among three are selected for each specimen geometry for the post-processing.

Tensile tests are conducted under extensometer-based strain control at a constant strain rate of $\dot{\varepsilon} = 10^{-3}\,\mathrm{s}^{-1}$. To this end, a temperature-resistant mechanical extensometer with a 25 mm gauge length is used. Fracture tests are also conducted in such a way to obtain the same strain rate employed for the tensile test. However, strain rate control cannot be used in ductile fracture test since the deformation is not homogeneous in the gauge length area of the extensometer. Indeed, the local strain rate at the fracture initiation site may be 10 times higher than in the rest of specimen. Therefore, the tests are carried out under displacement control at a constant crosshead velocity, which is set to obtain an average strain rate of $\dot{\varepsilon} = 10^{-3}\,\mathrm{s}^{-1}$.

The deformation evolution during experiments is recorded using Digital Image Correlation. To prepare specimens for DIC, the sample surface is cleaned and spray-painted with a white and black stochastic pattern using a spray can with acrylic paint. Two high speed cameras equipped with 50 mm lenses are used to acquire the images for the DIC. Despite the attention paid to ensure the alignment of the specimen with respect to the loading direction, a slight misalignment of the sample during the test is likely to occur in this kind of experiments, as was reported by Kacem et al.[40] and Tang et al.[41]. Indeed it is impossible to ensure a complete alignment during the test, and

even a slight misalignment will cause great rotation and asymmetry in the process of large plastic deformation leading to an asymmetrical strain distribution as was observed experimentally in many previous works (e.g. Lou et al. [34], Deole et al. [42] and Gruben et al. [43]). To account for this misalignment, five virtual extensometers with a gauge length of 15 mm are defined at different positions of the gauge area of specimen, using the DIC software Aramis [44] as shown in Fig.2 for the testing of a specimen with a central hole. Fig.2 shows also the evolution of the displacements of the five virtual extensometers in function of the normalized time. It can be observed that the displacement strongly depends on the position of the virtual extensometer. Therefore, for all specimen geometries, the values are averaged and the local displacement u corresponds then to the average of the displacements recorded by the five virtual extensometers.

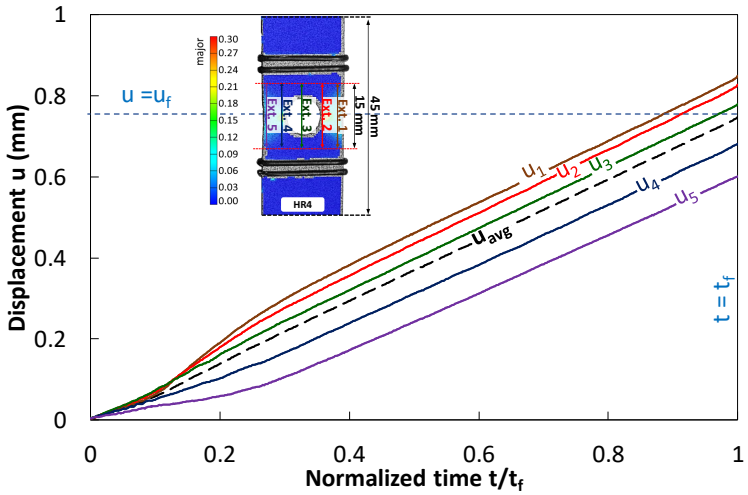

Figure 2: Evolution of displacement of the five virtual extensometers, with a gauge length of 15 mm, defined at different positions with DIC software as a function of time t normalized by the fracture time t_f, for a specimen with central hole HR4. The dashed black line depicts the average value of the five virtual extensometer displacements and u_f corresponds to the displacement at fracture.

2.3. Numerical models

Numerical simulations of the fracture tests are performed in 3D with the finite element code Abaqus/Standard. Since the strain is localized in the specimen center and DIC measures give the local displacement field, only a reduced part with a length L = 45 mm is modelled, as shown in Fig.3. In addition, to develop a FE model as close as possible to the experimental conditions, a model without symmetry conditions is defined to account for all possible displacements of the specimen during the test.

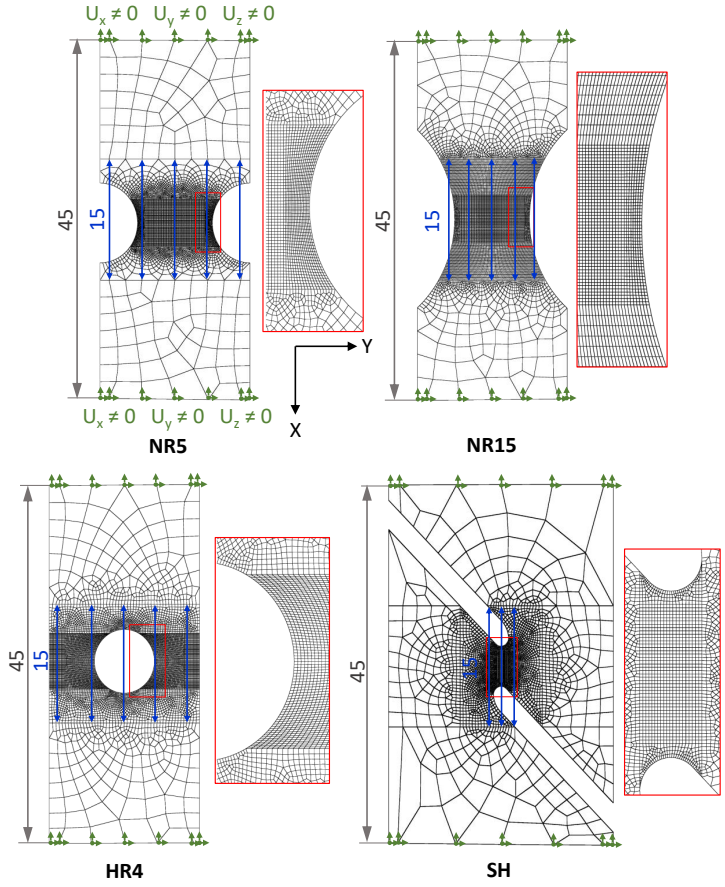

Figure 3: Meshes in X-Y plane and boundary conditions used for the four ductile fracture tests. Eight elements are defined through the thickness. The blue arrows highlight the position of the virtual extensometers with a gauge length of 15 mm used for local displacement measurement. All dimensions are in mm.

The region of interest is meshed using 3D solid hexahedral elements with reduced integration (C3D8R). A fine mesh is used in the local zone where strain localization is likely to occur and the size is increased at sections away from this zone. A mesh size of approximately 0.1 mm is applied to the fine

mesh area on the basis of a mesh sensitivity study showing that the effect of mesh size becomes insignificant when it is smaller than this value. Moreover, 8 layers of hexahedral elements are used through the thickness.

Recently, Kacem et al. [40] have shown that experimental boundary conditions have a significant effect on the fracture strain evaluation. Therefore, real non-zero displacement components (U_x, U_y and U_z) are imposed on the lower and upper sides of the specimen, with values derived from the experimental displacement field recorded by the DIC software at the same area, as shown in Fig.3. To this end, an automatic procedure is developed to apply the experimental local displacements to the FE model with a Python script as detailed in Appendix A. Such a procedure leads to a more realistic model, in which the misalignment of the specimen during the test is reproduced. For all simulations, isothermal conditions are assumed.

Isotropic hardening coupled with Hill48 yield criterion is chosen to model the mechanical behavior. The Hill48 quadratic yield function is given by:

$$f = \bar{\sigma} - \sigma_y\left(\bar{\varepsilon}_p\right) \tag{3}$$

where $\bar{\sigma}$ is the Hill48 equivalent stress that is defined as follow, from the components of the Cauchy stress tensor:

$$\bar{\sigma} = \sqrt{F\left(\sigma_{yy}-\sigma_{zz}\right)^2 + G\left(\sigma_{zz}-\sigma_{xx}\right)^2 + H\left(\sigma_{xx}-\sigma_{yy}\right)^2 + 2L{\sigma_{yz}}^2 + 2M{\sigma_{xz}}^2 + 2N{\sigma_{xy}}^2} \tag{4}$$

The Hill's coefficients (F, G, H, L, M and N) are related to the plastic anisotropy ratios, or r-values, (r_0, r_{45} and r_{90}) which are the ratios of the

width to thickness incremental plastic strain during a tensile test at 0 °, 45 ° and 90 ° to RD, respectively:

$$G = \frac{1}{1+r_0} \qquad H = Gr_0 \qquad F = \frac{Gr_0}{r_{90}} \qquad N = G\left(\frac{r_0}{r_{90}} + 1\right)(r_{45} + 0.5) \tag{5}$$

Due to the lack of available data regarding the mechanical behavior in the thickness of the sheet, L and M are kept equal to their isotropic value (i.e $L = M = 1.5$).

At elevated temperatures, the viscosity becomes significant. The strain rate dependency is commonly introduced as a power law in the isotropic hardening function σ_y, that is chosen with a saturation form of Hockett-Sherby, e.g. [45, 46]. Thus, the yield stress σ_y is defined at each temperature studied as a function of the strain rate $\dot{\varepsilon}$ as:

$$\sigma_y(\bar{\varepsilon}_p, \dot{\varepsilon}) = \left[\sigma_0 + Q\left(1 - exp\left(-b\left(\bar{\varepsilon}_p\right)^n\right)\right)\right]\left[\frac{\dot{\varepsilon}}{\dot{\varepsilon}_0}\right]^m \tag{6}$$

where $\bar{\varepsilon}_p$ is the equivalent plastic strain, σ_0 is the initial yield stress, Q represents the maximum change in the size of the yield surface, b defines the growth rate of the yield surface, n is the strain hardening coefficient, $\dot{\varepsilon}_0$ is a constant strain rate normalization factor and m is the strain rate sensitivity coefficient. It should be noted that for all strain rate below the strain rate normalization factor $\dot{\varepsilon}_0$, the yield stress σ_y is calculated only from the first bracketed term of Eq. 6. To define the hardening law in Abaqus, the stress-strain data are given as input in a tabular form at different strain rate levels.

2.4. Modeling and calibration of ductile fracture

2.4.1. Ductile fracture criterion

A stress state dependent ductile fracture criterion is used to determine the onset of the macroscopic fracture. This criterion characterizes the damage state in the material and when a critical value is reached, it leads to the onset of a macroscopical fracture. This criterion can be expressed according to the following general form:

$$D = \int_0^{\bar{\varepsilon}_f} \frac{d\bar{\varepsilon}_p}{\bar{\varepsilon}_f} \tag{7}$$

where D is a failure indicator that gives the onset of fracture at a given material point when it reaches unity and $\bar{\varepsilon}_f$ is the equivalent plastic strain to fracture (or fracture strain) that can be expressed according to Lou et al. [17, 18] as follows:

$$\bar{\varepsilon}_f = \frac{C_3}{\left(\frac{2}{\sqrt{L^2+3}}\right)^{C_1} \left(\frac{\langle 1+3\eta \rangle}{2}\right)^{C_2}} \tag{8}$$

C_1, C_2 and C_3 are three positive material parameters that need to be calibrated.

2.4.2. Calibration methodology

To calibrate the fracture material parameters, the equivalent plastic strain at the first element reaching $D=1$ at the instant of fracture t_f needs to be determined. However, this element cannot be located since the fracture parameters required to calculate D have not been identified yet. Therefore, it is assumed that the fracture initiates in the element with the highest equivalent plastic strain at the instant of fracture t_f (critical element). This

assumption had been checked and broadly applied in previous works. Indeed, Talebi-Ghadikolaee et al. [47] found that, in the case of notched specimens, the position of the element with the highest equivalent plastic strain is the same as that of the element with the highest failure indicator value. Lou and Huh [48] have shown that the element with the maximum failure indicator is close to the one with the largest equivalent plastic strain for specimen with central hole and shear specimen.

Moreover, in most experiments, fracture is not expected to initiate on the specimen surface making the direct measure of fracture strain through DIC impossible. Therefore, the hybrid experimental–numerical method is applied [36]. To this end, the displacement at fracture u_f is first determined experimentally at the instant of the sudden drop in the measured load-displacement curve. Subsequently, finite element simulations of ductile fracture tests are performed and the evolution of the equivalent plastic strain, stress triaxiality and Lode parameter are output. After verifying the agreement between experimental and numerical results, the maximum equivalent plastic strain is extracted from the numerical simulation of ductile fracture test at the corresponding experimental fracture stroke u_f. The evolution of stress triaxiality η and Lode parameter L at the critical element is also obtained from the numerical analysis, to account for the non-linearity in the loading path, when identifying the fracture parameters. Therefore, the failure indicator D at the critical element can be calculated for each test through Eq. 7.

Finally, to calibrate the fracture criterion, the fracture parameters are optimized using a generalized reduced gradient (GRG) algorithm tool by

minimizing the following cost function defined in the least square sense:

$$Erf = \sum_{i=1}^{N_s} (1 - D_i)^2 \tag{9}$$

where N_s denotes the number of samples used for the calibration and D_i corresponds to the failure indicator of the i^{th} test which is calculated numerically through Eq. 7.

3. Results and discussion

In this section, results of tensile and ductile fracture tests are presented and discussed. The effect of temperature on the stress state and fracture strain is investigated. The results of DF parameters calibration of the original Lou's DF at different temperatures are presented. Then the extended form of Lou's DF criterion is described. The ductile fracture locus obtained by the original and extended forms are compared to the experimental results.

3.1. Stress-strain curves

Cauchy stress-logarithmic strain curves at room and elevated temperatures (T = 150 °C and 200 °C) are obtained from tests performed on dog-bone specimen as shown in Fig.4. A representative curve is chosen among the three ones and it should be highlighted that very repeatable data are obtained for each temperature. The Cauchy stress is calculated by the ratio of the load over the current section of the sample before necking. The logarithmic strain is measured by the DIC software. The mechanical properties are given in Tab. 2. Constant values for elasticity parameters ($E = 70$ GPa and $\nu = 0.33$) are assumed for all tested temperatures.

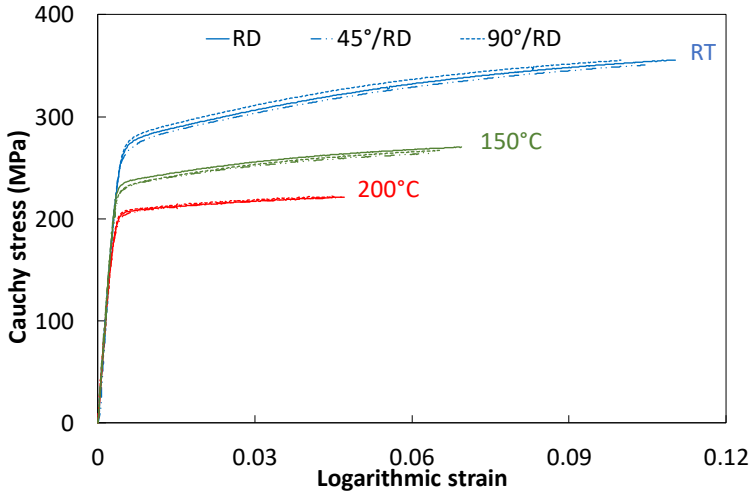

Figure 4: Cauchy stress-logarithmic strain curves of AA6061-T6 at $\dot{\varepsilon} = 10^{-3}\,\mathrm{s}^{-1}$ in uniaxial tension obtained with dog-bone specimen up to the point of necking at 0 °, 45 ° and 90 ° to the RD, at room temperature and at 150 °C and 200 °C.

	YS (MPa)	UTS (MPa)	r_0	r_{45}	r_{90}	$\bar{r}$	Δr
RT	270	318	0.59	0.78	0.81	0.74	-0.08
150 °C	235	252	0.59	0.66	0.72	0.66	-0.005
200 °C	205	211	0.64	0.71	0.72	0.7	-0.03

$\bar{r} = (r_0 + r_{90} + 2r_{45})/4 \qquad \Delta r = (r_0 + r_{90} - 2r_{45})/2$

Table 2: Mechanical properties in RD and anisotropy coefficients of AA6061-T6 at room temperature and at 150 °C and 200 °C.

It can be seen that, for all tested temperatures, there is no significant difference in stress-strain curves along different loading directions indicating isotropic properties with respect to strength and strain hardening, though

a slight gap recorded at RT that clearly disappears at higher temperatures. However, the flow behavior is significantly influenced by the temperature. As excepted, the Ultimate Tensile Stress (UTS) and the Yield Stress at 0.2 % plastic strain (YS) decrease with the temperature rise. For instance, UTS and YS decrease respectively by 33.6 % and 24.1 % when increasing the temperature from RT to 200 °C. It can be observed that the limit strain of the homogeneous deformation field decreases with increasing the temperature. This is due to the work hardening that decreases as the temperature increases leading to a faster occurrence of necking.

The measurement of both transverse and longitudinal strains leads to the calculation of the plastic anisotropy coefficients at 0 °, 45 ° and 90 °, also given in Tab. 2. These coefficients are determined by linear interpolation of the evolution of the plastic transverse strain versus the plastic thickness strain in the whole range of homogeneous deformation. The transverse strain is measured by DIC and the thickness strain is determined using the incompressibility condition; moreover, plastic components are calculated by removing the elastic part. Fig.5 shows the r-values evolution with the orientation from rolling direction at different testing temperatures. It is observed that for all temperatures, the value of the normal anisotropy coefficient is significantly different from 1, which indicates that the metal exhibits moderate anisotropy in plastic flow.

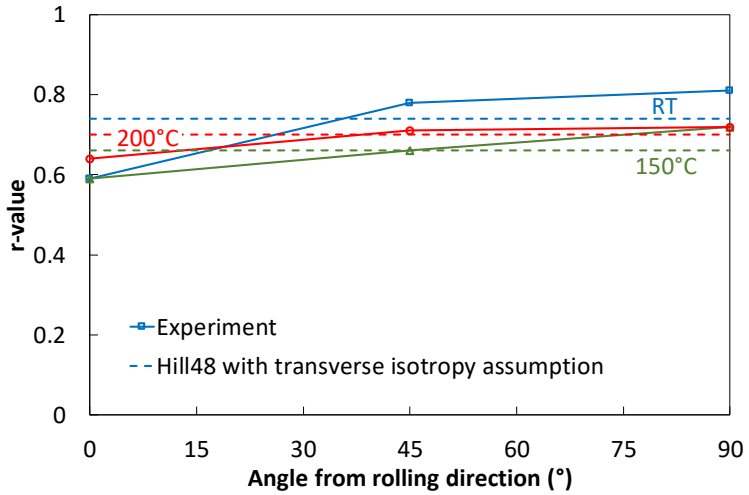

Figure 5: Plastic anisotropy coefficients (r-values), determined experimentally by the ratio of the plastic transverse strain to the plastic thickness strain in the whole range of homogeneous deformation, in function of orientation and temperature and comparison with the transverse isotropic Hill48 yield criterion calculated according to Eq.5 and considering only $\bar{r}$ (i.e. $r_0 = r_{45} = r_{90} = \bar{r}$).

3.2. Identification of mechanical behavior parameters

The Hill48 yield criterion parameters are identified directly from the r-values. Due to the very weak dependence of the stress-strain curve on the loading direction and the low value of the planar anisotropy coefficient Δr, transverse isotropy is assumed and the values of Hill48 coefficients, calculated according to Eq.5 and considering only $\bar{r}$ (i.e. $r_0 = r_{45} = r_{90} = \bar{r}$), are reported in Tab.3.

The hardening parameters are identified by inverse method. To this end, two strategies are commonly used. The first strategy consists in manually adjusting the unknown model parameters while visually checking the agreement

	F	G	H	N
RT	0.575	0.575	0.425	1.425
150 °C	0.602	0.602	0.398	1.398
200 °C	0.588	0.588	0.412	1.412

Table 3: Hill's coefficients calculated directly through r-values according to Eq.5 and considering only $\bar{r}$ (i.e. $r_0 = r_{45} = r_{90} = \bar{r}$) at room temperature and at 150 °C and 200 °C. L = M = 1.5

between experimental and numerical results. The second strategy consists in using an automatic process aiming at seeking for an optimal set of model parameters by minimizing an objective function value that defines the gap between experimental and numerical results. For its simplicity, the first strategy is used in this study. Indeed, the hardening parameters are continually adjusted until the numerical and experimental load-displacement curves obtained with all fracture specimens show good agreement as shown in Fig. 7. Tab. 4 shows the set of hardening parameters, obtained after several trial-and-error iterations and leading to the numerical results in Fig. 7. It should be noted that the hardening parameters are commonly identified based on the results of tensile test in the homogeneous strain range. After necking a classical approach consists in extrapolating the hardening curve up to a large strain range. Nevertheless, in this work, the hardening curve parameters are identified based on the load-displacement curves obtained with all fracture specimens up to fracture while checking the agreement between the experimental and numerical stress-strain curve obtained by tensile test in the

homogeneous strain range.

	σ_0 (MPa)	Q (MPa)	b	n	$\dot{\varepsilon}_0$ (s^{-1})	m
RT	244	135	7	0.68	–	–
150 °C	164	100	7	0.45	10^{-4}	0.031
200 °C	130	76	7	0.36	10^{-4}	0.04

Table 4: Hardening law parameters identified at room temperature and at 150 °C and 200 °C.

It should be also noted that in practice the strain rate sensitivity parameters (i.e. $\dot{\varepsilon}_0$ and m) are identified based on experimental results for different strain rates. However in this study experiments are conducted at only one strain rate value of $\dot{\varepsilon} = 10^{-3}\,s^{-1}$. Therefore these parameters are constrained to be as close as possible to the ones found in previous works for the same material grade [46]. Moreover, the strain hardening exponent n is assumed to evolve linearly with the temperature, as was reported previously by Laurent et al. [45] and the parameter b is fixed to be constant for all tested temperatures. It is found that both hardening parameters σ_0 and Q decrease with the temperature rise by about 45 %. The σ_0 parameter evolves in a linear manner with temperature. The strain rate parameter m increases with the temperature rise, indicating an increase of the positive strain rate sensitivity with temperature, as was also reported by Simoes et al. [49].

Fig. 6 shows the hardening curves obtained at $\dot{\varepsilon} = 10^{-3}\,s^{-1}$ and using the identified parameters as well as the hardening curve determined experimentally from the tensile tests. It is clearly seen that the calibrated Hockett-

Sherby gives a good prediction of the stress level at $\dot{\varepsilon} = 10^{-3}\,\mathrm{s}^{-1}$ within the limited strain range investigated with the tensile test.

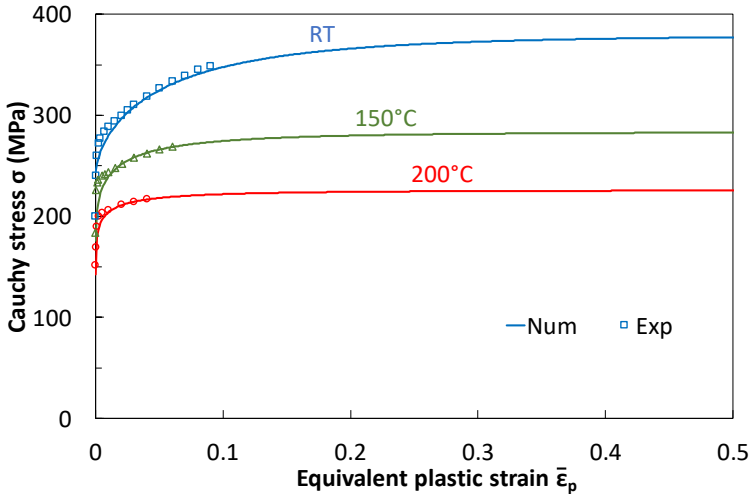

Figure 6: Hardening curves predicted by the modified Hockett-Sherby model at room temperature and at 150 °C and 200 °C (straight lines). Symbols represent experimental points obtained from uniaxial tension of dog-bone specimen at $\dot{\varepsilon} = 10^{-3}\,\mathrm{s}^{-1}$ in RD.

A comparison of the experimental and predicted load-local displacement curves is shown in Fig. 7 for the fracture tests. For clarity purpose, only one test per configuration is plotted.

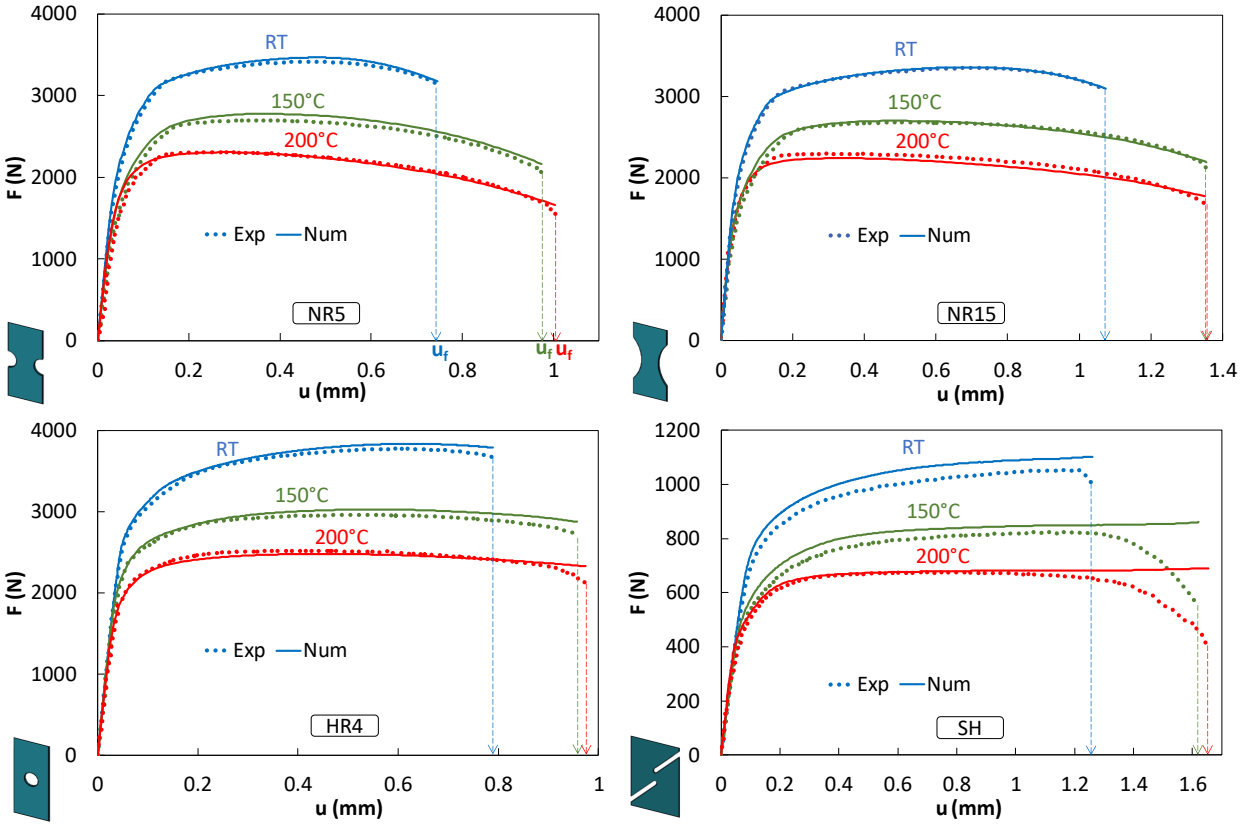

Figure 7: Numerical and experimental load-local displacement curves at room temperature and at 150 °C and 200 °C. Vertical dashed lines represent the displacement at fracture u_f. For clarity purpose, only one test per configuration is plotted.

Since this data is also used for the calibration, a good agreement is observed between numerical and experimental results. For shear test, a slight discrepancy of about 5 % is observed between experimental and numerical results at room temperature that decreases with the raise of temperature. This can be attributed to the lack of flexibility of the quadratic yield criterion used in this work characterized by too few anisotropic parameters as

was noticed by Bron and Besson [50]. This can be improved by using another yield function with more anisotropic parameters (e.g. Bron and Besson yield function [50] and Yld2004-18p [51]) as was reported by Zhang et al. [52]. It should be noted that in a previous work conducted for the same material at room temperature [40], the load-local displacement curves in Fig. 7 are also obtained numerically and experimentally for the same specimen geometries but with neglecting the anisotropy and the strain rate dependency. However, in this previous work, the shear specimen is used to identify the hardening curve after necking. Therefore, a good agreement is obtained between experimental and numerical results for the shear specimen but a slight difference is observed in the case of notched specimen NR5.

It is found out that the temperature affects strongly the maximum load F_{max}, namely it decreases with increasing temperature for all specimen geometries. At constant temperature, the force levels between both notched specimens are quite similar while it is slightly larger for HR4 specimen and drops significantly for the SH specimen. Indeed, at room temperature, the maximum load is found to be respectively 3422 N and 3356 N for notched specimens NR5 and NR15, 3791 N for HR4 specimen and 1069 N for SH specimen. At elevated temperatures, the same trend is recorded. Also, it can be seen that the maximum load is more rapidly reached at elevated temperatures. For instance, for NR5 specimen, F_{max} is reached at 66 % u_f and 23 % u_f for RT and 200 °C, respectively. This is due to the localized necking that appears earlier at elevated temperatures.

The numerical simulations are also verified by comparing the major strain distribution just before fracture and the evolution of the average major strain

on the surface of the critical zone, where the fracture is most likely to occur for each specimen as illustrated in Fig. 8. For elevated temperatures, experimental results are not plotted until fracture because the speckles spray-painted on the surface of the critical zone of specimen peeled off due to the high temperature and the large deformation prior to fracture, thus making impossible the DIC computation. Only major strain distribution at RT are plotted in Fig. 8 since DIC results are not available just before fracture. It can be seen that the numerical results fit well the experimental ones. The asymmetrical experimental strain distribution, coming from the misalignment of the specimen during the test, is also well predicted by the numerical model for all tested specimens and temperatures. The maximum major strain is found close to the edge for NR5 specimen and close to the center for NR15 specimen. For HR4 specimen, the major strain is concentrated on the right side of the hole edge. For SH specimen, the maximum major strain is located close to the edge where fracture experimentally initiates.

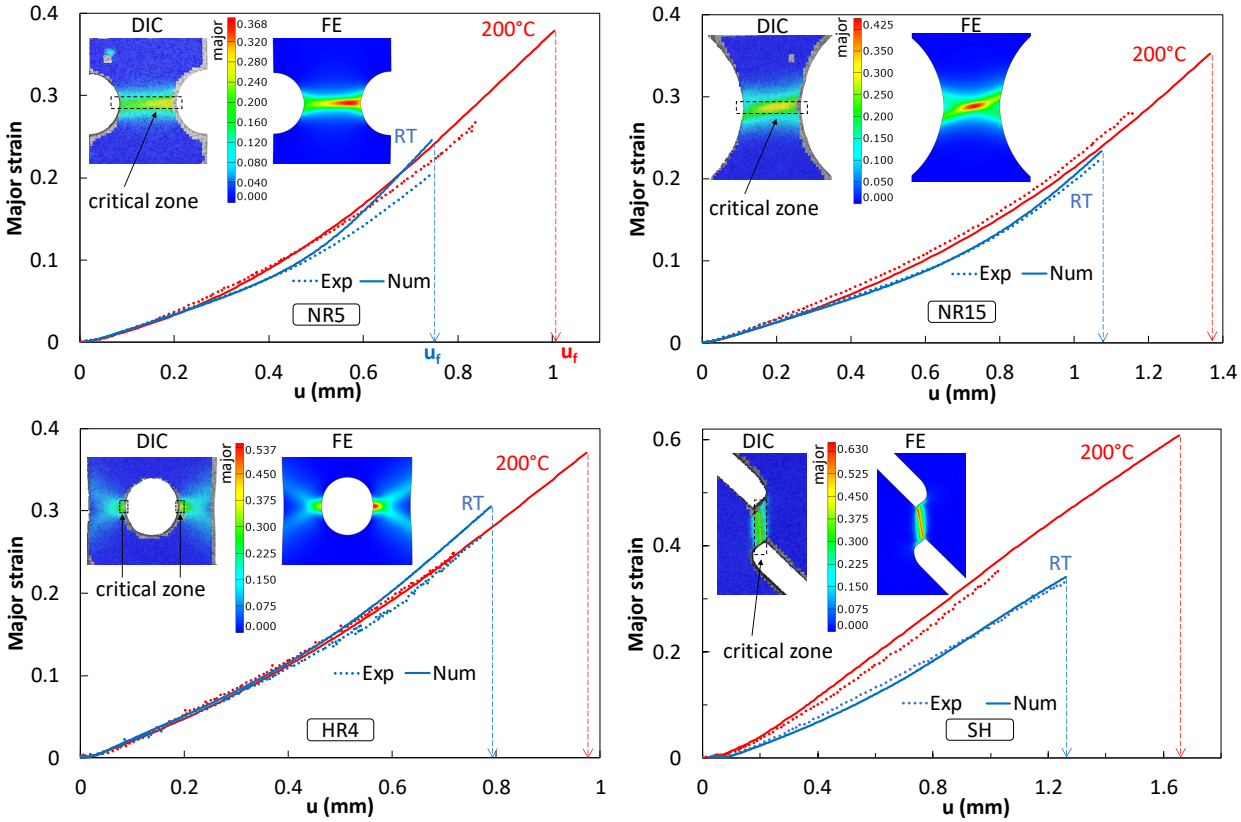

Figure 8: Comparison of major strain distribution on the specimen surface between DIC and FE simulation just before fracture at room temperature and the evolution of the average major strain on the surface of the critical zone where the fracture is likely to occur at room temperature and 200 °C. Vertical dashed lines represent the displacement at fracture u_f. Experimental results are not plotted until fracture at 200°C because the speckles spray-painted on the surface of the critical zone of specimen peeled off due to the high temperature.

3.3. Effect of temperature on the stress state and fracture strain

Hybrid experimental-numerical approach is used to determine the fracture strain and the evolution of the stress state parameters (η and L) until the

fracture initiation. Fig. 7 shows the displacement at fracture u_f determined at the instant of the sudden drop in the measured load-displacement curve for NR5, NR15 and HR4 specimens. For SH specimen, the load-displacement curve gradually drops before fracture making the determination of u_f in this way more difficult. Therefore, a novel method that makes use of the load first derivative is adopted [29]. In this case, the fracture stroke is identified at the minimum of this curve as shown in Fig. 9.

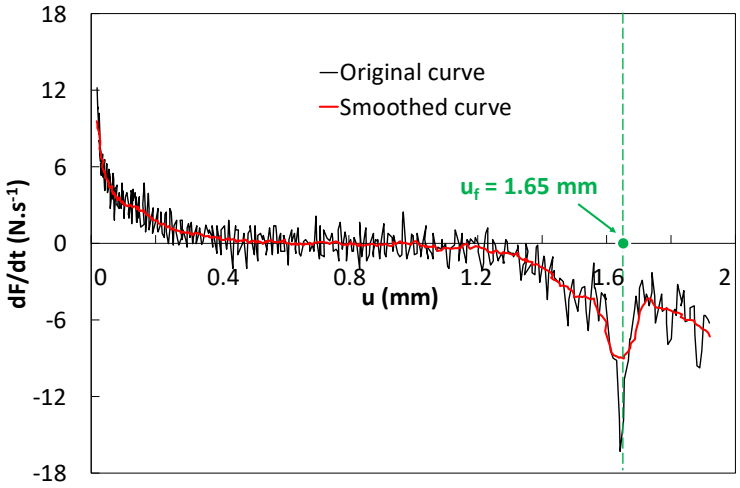

Figure 9: Original (in black) and smoothed (in red) load first derivative-local displacement curves of the shear specimen at 200 °C. Vertical dashed lines depict the minimum of the smoothed curve corresponding to the displacement at fracture u_f.

It can be seen that the displacement at fracture depends strongly on the specimen geometry. The maximum value of u_f is obtained with the SH specimen while the minimum value with NR5 and HR4 specimens. The temperature affects also the displacement at fracture u_f with less effect beyond 150 °C. For instance, for NR5 specimen, u_f rises by 31% when increasing the

temperature from RT to 150 °C while it rises by 4.7% when increasing the temperature from 150 °C to 200 °C. The value of u_f remains quite constant when increasing the temperature from 150 °C to 200 °C for NR15 and HR4 specimens.

Fig. 10 shows the location of the element with the maximum equivalent plastic strain at u_f. It is found that the critical element is located within the thickness for NR5, NR15 and HR4 specimens. For SH specimen, due to the edge effect, the maximum equivalent plastic strain at u_f is observed at the edge for all tested temperatures. However, the stress state is not characteristic of shear in this region. Therefore, the central element of the shear gauge is chosen as the critical element rather than the element at the edge. It is also found out that the location of the critical element is insensitive to the temperature. Experimentally, when inspecting visually the specimen after fracture, it was found that the fracture initiates close to the location of maximum equivalent plastic strain.

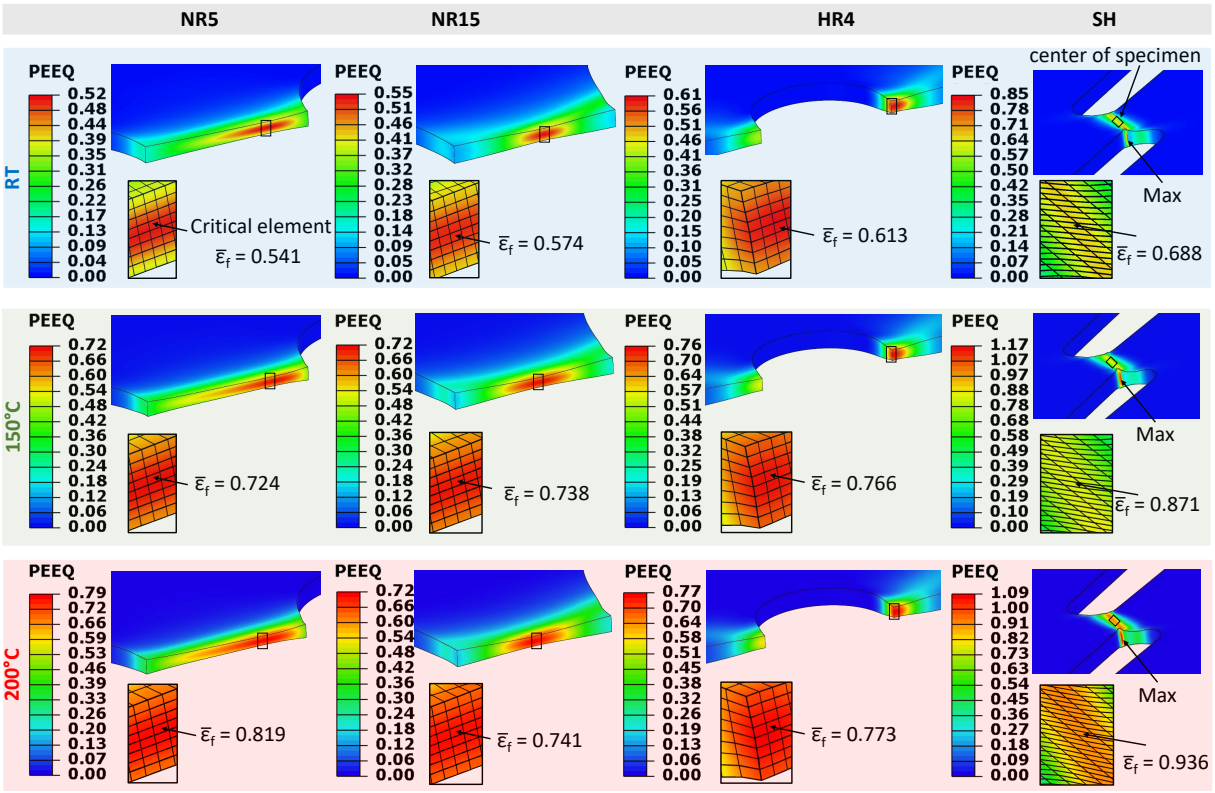

Figure 10: Contour plot of the equivalent plastic strain at the onset of fracture in the critical zone for different ductile fracture tests at room temperature and at 150 °C and 200 °C. Arrows in the zoomed pictures show the element with the maximum equivalent plastic strain corresponding to the critical element for NR5, NR15 and HR4 specimens and the element at the center of the specimen corresponding to the critical element for SH specimen. Note that the fracture strain $\bar{\varepsilon}_f$ corresponds to the value of the equivalent plastic strain at the integration point of the critical element. Only one of the two post-processed tests per configuration is presented.

To visualize the loading paths to fracture, Fig. 11 shows the evolution of stress triaxiality and Lode parameter calculated at the critical element as a function of the equivalent plastic strain and temperature for each specimen

type.

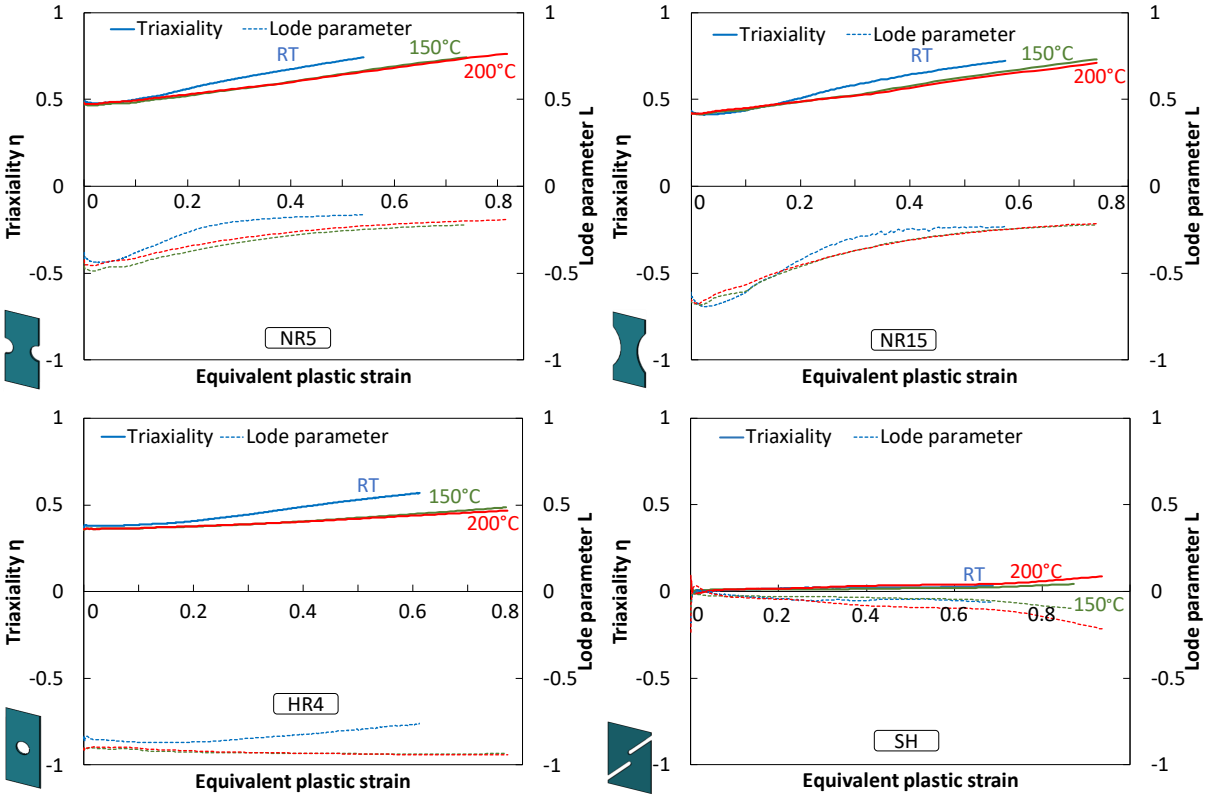

Figure 11: Evolution of stress triaxiality and Lode parameter at the critical element corresponding to the element presenting the maximum equivalent plastic strain at the displacement at fracture u_f for NR5, NR15 and HR4 specimens and selected at the center of the shear gauge for SH specimen. Only one of the two post-processed tests per configuration is plotted.

It is observed that the stress triaxiality values covered by the experiments are positive, ranging from 0 up to 0.75, while negative values of Lode parameters ranging from -1 up to 0 are obtained. Although specimens are designed to achieve a constant stress state, it is found that regardless of the

testing temperature the values of stress state parameters show significant variation during plastic deformation, especially for the notched specimens. This is due to the localized necking leading to the development of out of plane stress components in the critical zone that increases the stress triaxiality and modifies the evolution of Lode parameter. For NR5 specimens at RT, the stress triaxiality rises from 0.48 at the start of plastic deformation up to 0.71 at the fracture initiation. For NR15 specimens at RT, the stress triaxiality increases from 0.42 to 0.72. Quite similar values at the start and the end of deformation are also obtained at 150 °C and 200 °C. However, the stress triaxiality rises more rapidly at RT since the plastic deformation at fracture is lower than the one obtained at elevated temperatures. The same trend is also observed for the Lode parameter, respectively rising from -0.38 to -0.17 and from -0.62 to -0.2 for NR5 and NR15 specimens at RT. For HR4 specimen, the variation of stress state parameters is smaller than the one of notched specimens, since only a weak necking occurs. At RT, the stress triaxiality and Lode parameter increase respectively from 0.36 to 0.52 and from -0.86 to -0.82. However, nearly constant values are observed at elevated temperatures. For SH specimen, a perfect pure shear state, corresponding to $\eta = 0$ and $L = 0$, is not obtained but the values of η and L are nearly constant and close to zero.

Since stress state parameters are evolving during deformation, it is convenient to assign a specific stress state to each fracture test by using the average of stress triaxiality η_{avg} and Lode parameter L_{avg} calculated by the following relations:

$$\eta_{avg} = \frac{1}{\bar{\varepsilon}_f} \int_0^{\bar{\varepsilon}_f} \eta \, d\bar{\varepsilon}_p \quad \text{and} \quad L_{avg} = \frac{1}{\bar{\varepsilon}_f} \int_0^{\bar{\varepsilon}_f} L \, d\bar{\varepsilon}_p \tag{10}$$

Tab.5 shows the values of the fracture strain $\bar{\varepsilon}_f$ and the corresponding average triaxiality η_{avg} and Lode parameter L_{avg}.

		$\bar{\varepsilon}_f$	η_{avg}	L_{avg}
NR5	RT	0.469 ± 0.072	0.584 ± 0.019	-0.27 ± 0.011
	150 °C	0.697 ± 0.028	0.585 ± 0.01	-0.339 ± 0.019
	200 °C	0.807 ± 0.013	0.609 ± 0.003	-0.287 ± 0.002
NR15	RT	0.56 ± 0.015	0.563 ± 0.003	-0.382 ± 0.004
	150 °C	0.703 ± 0.036	0.558 ± 0.008	-0.382 ± 0.006
	200 °C	0.739 ± 0.003	0.562 ± 0.002	-0.366 ± 0.002
HR4	RT	0.576 ± 0.038	0.428 ± 0.029	-0.869 ± 0.035
	150 °C	0.739 ± 0.028	0.408 ± 0.003	-0.93 ± 0.001
	200 °C	0.74 ± 0.034	0.376 ± 0.031	-0.931 ± 0.004
SH	RT	0.655 ± 0.034	0.021 ± 0.002	-0.047 ± 0.005
	150 °C	0.857 ± 0.014	0.017 ± 0.002	-0.039 ± 0.005
	200 °C	0.901 ± 0.036	0.038 ± 0.003	-0.093 ± 0.004

Table 5: Fracture strain and the corresponding average stress triaxiality and Lode parameter with the absolute uncertainty at room temperature and at 150 °C and 200 °C. The absolute uncertainty is calculated based on the two post-processed tests for each geometry and temperature.

It can be seen that the fracture strain is strongly dependent on the stress state and temperature. The fracture strain may increase by more than a

factor of 1.7 when increasing the temperature from RT to 200 °C (for NR5 specimen) or by more than a factor of 1.4 when decreasing the stress triaxialilty value from 0.58 to 0.02 (at RT).

Fig. 12 shows the evolution of η_{avg} and L_{avg} as a function of temperature. It can be seen that the temperature has less effect in case of the notched specimen NR15 where η_{avg} and L_{avg} remain at constant values respectively of about 0.56 and -0.38 regardless of the testing temperature. However, the stress state of the other specimens depends slightly on the testing temperature. For instance, for HR4 specimen, η_{avg} and L_{avg} decreases by about 0.05 when increasing the temperature from RT to 200 °C. Therefore, It can be stated that the temperature effect on the stress state is rather small and depends on the specimen geometry.

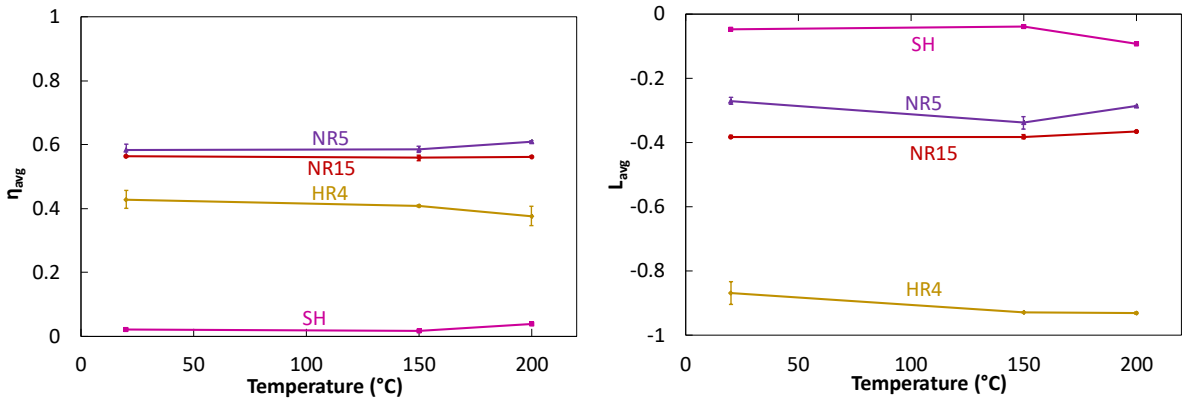

Figure 12: Evolution of the average triaxiality η_{avg} and Lode parameter L_{avg}, calculated according to Eq.10, as a function of temperature for all fracture specimens. Error bars depict the maximum and minimum values of the two post-processed tests for each geometry and temperature.

3.4. Prediction of ductile fracture

The ductile fracture criterion used in this study depends on three parameters (C_1, C_2 and C_3) that have to be identified using the procedure described in 2.4.2 to derive the fracture locus. Calibration is performed by using all the post-treated tests for each temperature (i.e. $N_s = 4\text{x}2{=}8$). Tab.6 shows the calibration results. Fig.13 shows the evolution of the calibrated fracture parameters as a function of temperature.

	C_1	C_2	C_3
RT	0.6398	0.2500	0.6118
150 °C	0.0877	0.2130	0.7562
200 °C	0	0.1662	0.8009

Table 6: Calibrated fracture parameters of Lou's ductile fracture criterion at RT, 150 °C and 200 °C.

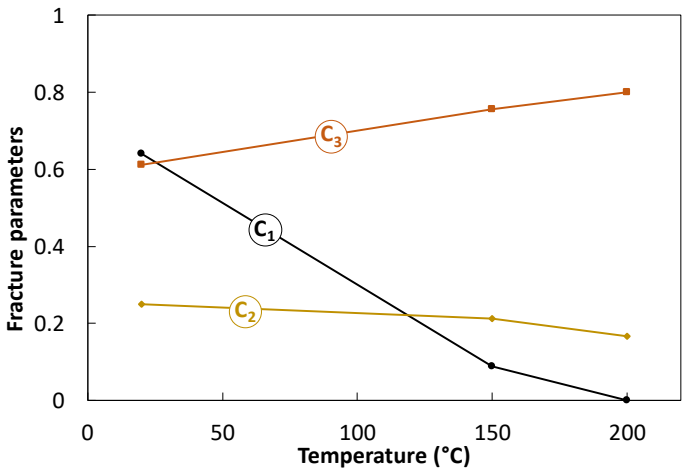

Figure 13: Evolution of the three calibrated Lou's fracture parameters (C_1, C_2 and C_3) as a function of temperature.

It can be seen that the value of C_1, which modulates the effect of the Lode parameter, is small compared to the values found in literature (e.g. $C_1 = 3.3845$ for AA6082-T6 [34] and $C_1 = 2.8703$ for AA6016-T4 [35] at RT) for all tested temperatures. This indicates a weak Lode parameter dependence for this material, notably at elevated temperatures, that was also noted in previous studies for AA5083-H116 [53] and AA5083-O [54] aluminum alloys at RT. The values of the fracture parameter C_2, which modulates the effect of the stress triaxiality, indicates a moderate stress triaxiality sensitivity that decreases with increasing temperature in agreement with the results of Pantousa et al. [55] for steel. As expected, the parameter C_3, which indicates the overall level of fracture strain and corresponds theoretically to the fracture strain in uniaxial tension, increases with the temperature rise. Indeed, C_3 increases by 31% when increasing the temperature from RT to 200 °C. It should be noted that the calibrated values obtained at RT in this study are slightly different from those found out in a previous work for the same material grade ($C_1 = 0.1588$, $C_2 = 0.5725$ and $C_3 = 0.4593$) [40], since the anisotropy is considered and more tests are used for calibration.

Fig.14 shows the fracture loci resulting from the calibration of the DF criterion corresponding to the plot of fracture strain as the function of the stress triaxiality and the Lode parameter. The symbols represent the fracture strain obtained by the hybrid approach with their corresponding average stress triaxiality and Lode parameter.

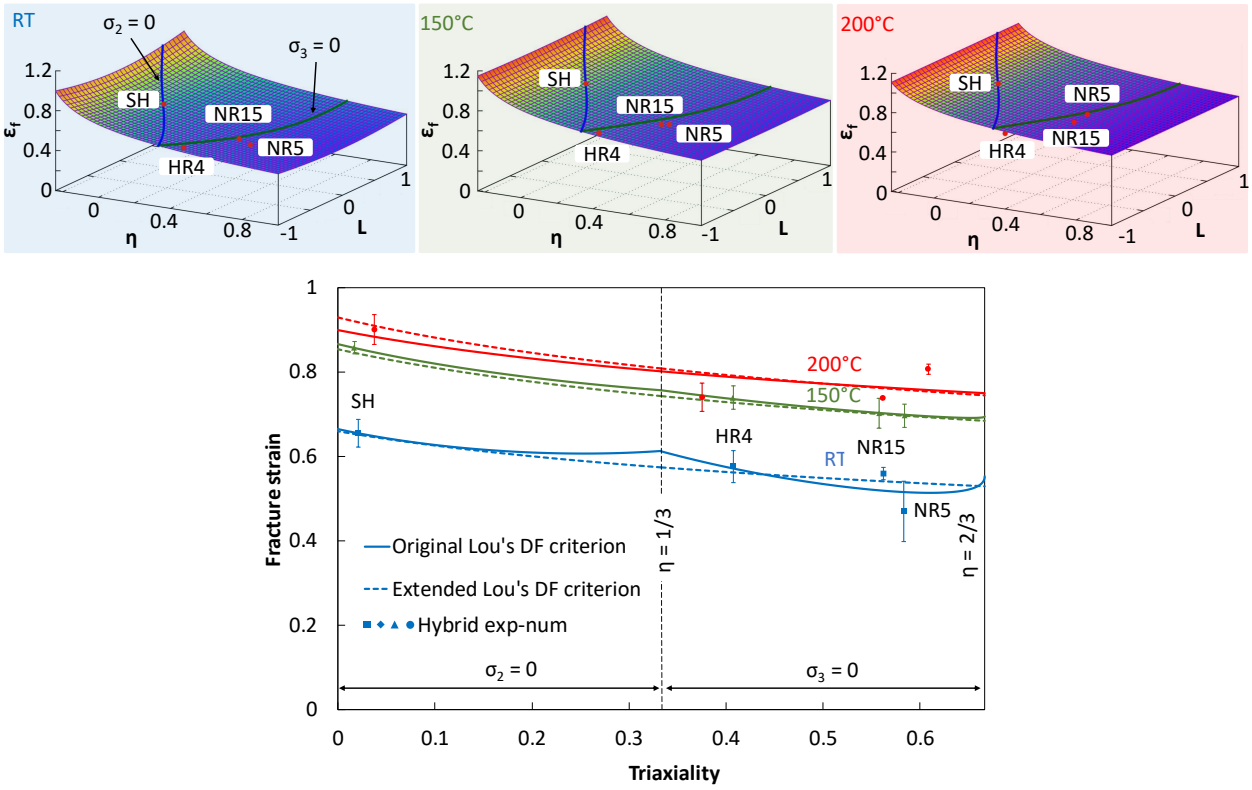

Figure 14: Fracture locus of AA6061-T6 constructed in the space of stress triaxiality, Lode parameter and equivalent plastic strain by the original Lou's DF criterion (top of the figure) and in the space of stress triaxiality and equivalent plastic strain under plane stress by the original and extended Lou's DF criterion (lower part of the figure) at RT, 150 °C and 200 °C. Dots with corresponding error bars represent (η_{avg}, $\bar{\varepsilon}_f$) points obtained by the hybrid experimental-numerical approach. Error bars depict the maximum and minimum values of fracture strain $\bar{\varepsilon}_f$ of the two post-processed tests for each geometry and temperature.

The overall shape of the fracture loci obtained at 150 °C and 200 °C in the top part of the figure is similar, where an evident stress triaxiality dependence and weak Lode parameter dependence are observed. The shape of

the fracture locus obtained at RT is slightly different from the one obtained at elevated temperatures, where a much stronger dependence on the stress triaxiality and on the Lode parameter is seen. This is clearly seen in the lower part of the figure, where the fracture loci are plotted under the plane stress condition in the space of stress triaxiality and equivalent plastic strain. It should be noted that a much stronger dependence of the fracture surface on the stress state and temperature has been observed for other materials as was found, for instance, by Pandya et al. [56] for AA7075-W.

The (η_{avg}, $\bar{\varepsilon}_f$) points obtained by the hybrid experimental approach are superimposed in Fig.14. It can be seen that globally the locus fits all the data points obtained by the hybrid approach quite well. To evaluate more precisely the prediction accuracy of DF criterion parameters an error indicator is used:

$$\delta = \frac{|D_{cri} - D_{pred}|}{D_{cri}}.100\% \tag{11}$$

where D_{cri} is the critical value of D which is supposed to be one in this work and D_{pred} is the value of D in the critical element at the fracture stroke.

Tab.7 shows the prediction error for the ductile fracture criterion calibration at room and elevated temperatures.

		NR5	NR15	HR4	SH
RT	D_{pred}	0.9027	1.0601	0.9929	1.0014
	error (%)	9.73	6.01	0.71	0.14
	mean error (%)	**4.15**			
150 °C	D_{pred}	0.9957	0.9979	0.9998	1.0005
	error (%)	0.44	0.21	0.02	0.05
	mean error (%)	**0.18**			
200 °C	D_{pred}	1.0655	0.9670	0.9332	1.0199
	error (%)	6.55	3.30	6.68	1.99
	mean error (%)	**4.63**			

Table 7: Failure indicator D predicted in the critical element at the fracture stroke by Lou's DF criterion and prediction errors (Eq.11).

It is found that the mean errors of the three tested temperatures are small (lower than 5%) notably at 150 °C, where the predicted results fit perfectly the experimental ones. Therefore, it can be concluded that Lou's ductile fracture criterion widely used in previous works to predict DF initiation at room temperature (e.g. [42, 57]) is also well suited to predict accurately DF at elevated temperatures.

3.5. Extension of Lou's ductile fracture criterion

Industrial warm forming operations are usually conducted under non-isothermal conditions. However, the DF parameters are identified for a limited isothermal conditions. To overcome this limitation, in this section, an extension of Lou's DF criterion is proposed by adding a new parameter to include the effect of temperature on the DF prediction.

Fig.15 shows the evolution of the predicted fracture strain by Lou's ductile fracture criterion with temperature for different stress states.

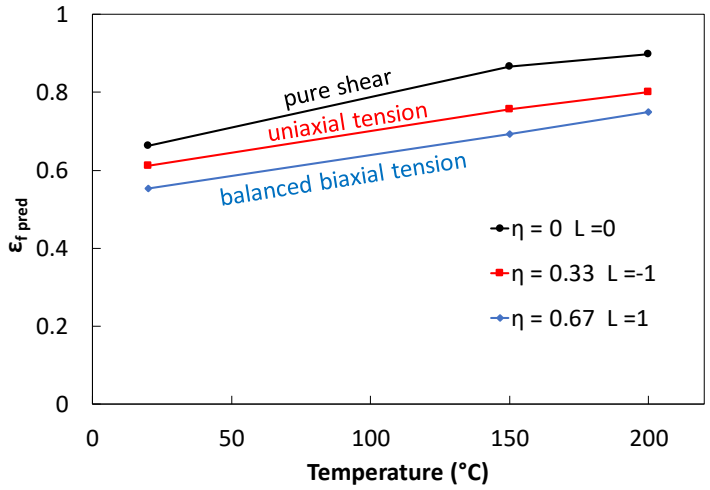

Figure 15: Evolution of fracture strain predicted by the original Lou's DF criterion with the calibrated material parameters given in Tab.6 versus temperature for three different stress states of pure shear ($\eta = 0$, $L = 0$), uniaxial tension ($\eta = 0.33$, $L = -1$) and balanced biaxial tension ($\eta = 0.67$, $L = 1$).

It can be seen that the predicted fracture strain gradually changes in an approximately linear way for all stress states. The same trend was also noted in [26], and a ductile fracture model was developed, based on multiplicative contributions considering the effects of stress state, strain rate and temperature:

$$\bar{\varepsilon}_f = [C_5 + C_6\ exp(C_7\ \eta)]\ [1 + C_8\ ln(\dot{\varepsilon}/\dot{\varepsilon}_0)]\ [1 + C_9\ T^*] \tag{12}$$

where C_5 to C_9 denotes the Johnson-Cook fracture parameters and T^* is the homologous temperature, defined by :

$$T^* = \frac{T - T_{ref}}{T_m - T_{ref}} \tag{13}$$

T_{ref} and T_m are reference and melting temperature, respectively ($T_{ref} = 293\,\mathrm{K}$ and $T_m = 873\,\mathrm{K}$). The expressions in the first, second and third sets of brackets represent respectively the effects of triaxiality (stress state), strain rate and temperature.

In the same way, to reflect the effect of temperature, the original Lou's ductile fracture criterion (Eq.8) is multiplied by the linear temperature term in the Johnson-Cook criterion leading to the following expression for the fracture strain:

$$\bar{\varepsilon}_f(T) = \frac{C_3}{\left(\frac{2}{\sqrt{L^2+3}}\right)^{C_1} \left(\frac{\langle 1+3\eta \rangle}{2}\right)^{C_2}} \left(1 + C_4\ T^*\right) \tag{14}$$

Accordingly, the extended form of Lou's ductile fracture criterion is expressed as:

$$D(T) = \frac{1}{C_3(1 + C_4\ T^*)} \int_0^{\bar{\varepsilon}_f} \left(\frac{2}{\sqrt{L^2+3}}\right)^{C_1} \left(\frac{\langle 1+3\eta \rangle}{2}\right)^{C_2} d\bar{\varepsilon}_p \tag{15}$$

It should be noted that the strain rate dependence of fracture strain is not considered in this work. For that reason the linear strain rate term in the Johnson-Cook model is omitted in the extended form of Lou's DF criterion. It should be also recalled that to avoid the influence of strain rate on ductile fracture, the cross head speed in fracture tests is optimized to ensure the same strain rate for all fracture specimens.

The extended form of Lou's ductile fracture criterion involves three parameters (C_1, C_2 and C_3) and an additional one C_4 to include the influence

of temperature. Since the material used in this work exhibits a weak Lode parameter dependency, the value of C_1 is set equal to zero. The remaining parameters are identified by using the procedure described in 2.4.2 based on all post-processed tests (i.e. $N_s = 4\text{x}2\text{x}3{=}24$). The identified values are $C_2 = 0.201$, $C_3 = 0.573$ and $C_4 = 1.321$.

The fracture loci obtained with this calibrated model are superimposed in Fig.14 in the space of stress triaxiality and equivalent plastic strain. It is observed that the fracture loci obtained with the extended form of DF criterion is close to the original form especially at elevated temperatures. Tab 8 shows the prediction error for the extended DF calibration at room and elevated temperatures.

		NR5	NR15	HR4	SH
RT	D_{pred}	0.873	1.035	1.032	1.006
	error (%)	12.73	3.54	3.17	0.61
	mean error (%)	**5.01**			
150 °	D_{pred}	0.999	1.002	1.015	1.014
	error (%)	0.09	0.23	1.53	1.39
	mean error (%)	**0.81**			
200 °	D_{pred}	1.069	0.968	0.927	0.990
	error (%)	6.90	3.17	7.28	0.93
	mean error (%)	**4.57**			

Table 8: Failure indicator D predicted in the critical element at the fracture stroke by the extended Lou's DF criterion and prediction errors (Eq.11).

It is found that the mean errors of the three tested temperatures are small and in the same range of those obtained by the original model. Indeed the

mean error for all tested temperature is found to be 3.46 %, which is very close to the one obtained with the original model, about 3 %. These results validate the extended form of DF criterion, which is very useful to predict DF initiation under non-isothermal conditions usually encountered in warm forming.

4. Conclusions

To figure out the relationship between forming limits, stress state and temperature, ductile fracture prediction of AA6061-T6 aluminum alloy sheet metal is investigated at room and elevated temperatures under a wide stress state range. Specimens with different shapes are manufactured and deformed to achieve different stress states at RT, 150 °C and 200 °C. The hybrid experimental-numerical approach is used to identify the fracture strain and the corresponding stress state parameters (i.e. stress triaxiality and Lode parameter). To accurately model the ductile fracture experiments, the FE model is constrained by the real experimental boundary conditions and a strain rate dependent anisotropic material model is employed. The comparison of the experimental and numerical results in terms of both force-displacement curves and major strain distribution clearly demonstrates the capability of the model to predict accurately the material response in different loading conditions. Lou's DF criterion is used to consider the influence of the stress parameters on the ductile fracture behavior. The DF is also extended to add the dependence of temperature.

It is found out that the fracture strain is strongly dependent on the stress state and temperature. The fracture strain may increase by more than a

factor of 1.7 when increasing the temperature from RT to 200 °C or by more than a factor of 1.4 when decreasing the stress triaxialilty value from 0.58 to 0.02.

It is also found out that the temperature effect on the stress triaxiality is rather small and depends on the specimen geometry. The temperature has less effect in case of the notched specimen NR15. However, the stress state of the other specimens depends slightly on the testing temperature.

Also, results indicate that AA6061-T6 aluminum alloy exhibits a weak Lode parameter dependency regardless of the tested temperature while a moderate stress triaxiality sensitivity that decreases with the temperature rise is noted. Moreover, the overall level of fracture strain increases by 31% when temperature increases from RT to 200 °C.

The predictive capabilities of the original and extended criteria is evaluated using an error indicator. The mean error for all tested temperature is found to be 3 % and 3.46 % for the original and extended criteria, respectively. Therefore, it can be stated that Lou's DF criterion is well suited to predict accurately ductile fracture at elevated temperatures under isothermal conditions whereas the extended form of Lou's DF criterion is very useful to predict DF initiation under non-isothermal conditions usually encountered in warm forming.

Acknowledgements

The authors acknowledge the Région Bretagne financial support with the SAD18037 program.

Appendix A. Procedure to apply the real experimental boundary conditions in Abaqus

Fig.A shows the flowchart of the Python script used to define the boundary conditions in Abaqus from the experimental DIC results. The experimental local displacement filed on the surface of specimen is recorded during test by the DIC software Aramis. Firstly, a reduced part of specimen with a length L = 45 mm is defined in the specimen center. Then, a total of ten points i are selected in the upper and lower sides of the reduced part of specimen. The coordinates (X_i, Y_i, Z_i) of the selected points are extracted at each time stage t. The initial coordinates (X_{i0}, Y_{i0}) determined at the first stage ($t = t_0$) are used to define the 2D initial mesh in Abaqus that was then extruded in the thickness direction to give the 3D mesh. Finally, the experimental displacements calculated at the selected points (U_{xi}, U_{yi}, U_{zi}) are applied to the corresponding node sets to define the boundary conditions in Abaqus.

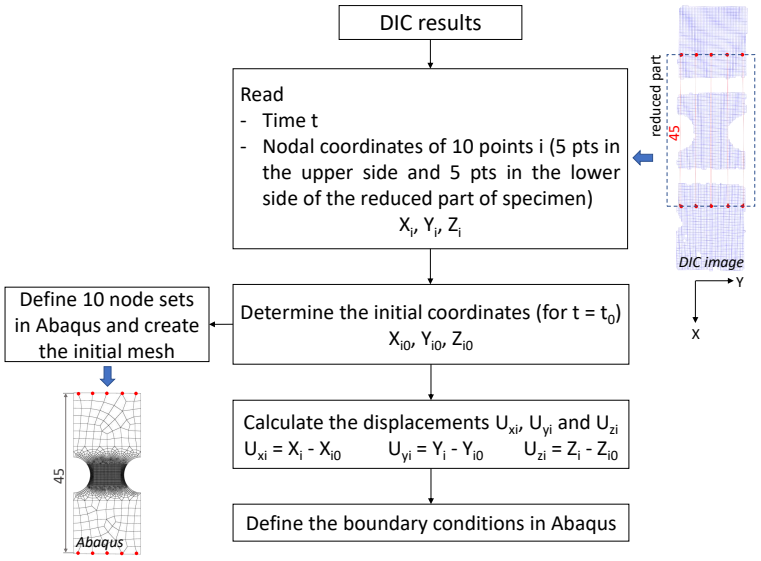

Figure A: Flowchart of the python script for applying the experimental local displacement, obtained from DIC results, to the FE model.

References

[1] J. Hancock, A. Mackenzie, On the mechanisms of ductile failure in high-strength steels subjected to multi-axial stress-states, Journal of the Mechanics and Physics of Solids 24 (2-3) (1976) 147–160. doi:10.1016/0022-5096(76)90024-7.

[2] M. S. Mirza, D. C. Barton, P. Church, The effect of stress triaxiality and strain-rate on the fracture characteristics of ductile metals, Journal of Materials Science 31 (2) (1996) 453–461. doi:10.1007/bf01139164.

[3] Y. Bao, T. Wierzbicki, On fracture locus in the equivalent strain and

stress triaxiality space, International Journal of Mechanical Sciences 46 (1) (2004) 81–98. doi:10.1016/j.ijmecsci.2004.02.006.

[4] K. Zhang, J. Bai, D. François, Numerical analysis of the influence of the lode parameter on void growth, International Journal of Solids and Structures 38 (32-33) (2001) 5847–5856. doi:10.1016/s0020-7683(00)00391-7.

[5] T. Wierzbicki, Y. Bao, Y.-W. Lee, Y. Bai, Calibration and evaluation of seven fracture models, International Journal of Mechanical Sciences 47 (4-5) (2005) 719–743. doi:10.1016/j.ijmecsci.2005.03.003.

[6] X. Gao, J. Kim, Modeling of ductile fracture: Significance of void coalescence, International Journal of Solids and Structures 43 (20) (2006) 6277–6293. doi:10.1016/j.ijsolstr.2005.08.008.

[7] F. Shehata, M. Painter, R. Pearce, Warm forming of aluminium/magnesium alloy sheet, Journal of Mechanical Working Technology 2 (3) (1978) 279–290. doi:10.1016/0378-3804(78)90023-2.

[8] R. A. Ayres, M. L. Wenner, Strain and strain-rate hardening effects in punch stretching of 5182-0 aluminum at elevated temperatures, Metallurgical Transactions A 10 (1) (1979) 41–46. doi:10.1007/bf02686404.

[9] A. H. Clausen, T. Børvik, O. S. Hopperstad, A. Benallal, Flow and fracture characteristics of aluminium alloy AA5083–h116 as function of strain rate, temperature and triaxiality, Materials Science and Engineering: A 364 (1-2) (2004) 260–272. doi:10.1016/j.msea.2003.08.027.

[10] D. Li, A. K. Ghosh, Biaxial warm forming behavior of aluminum sheet alloys, Journal of Materials Processing Technology 145 (3) (2004) 281–293. doi:10.1016/j.jmatprotec.2003.07.003.

[11] S. Mahabunphachai, M. Koç, Investigations on forming of aluminum 5052 and 6061 sheet alloys at warm temperatures, Materials & Design (1980-2015) 31 (5) (2010) 2422–2434. doi:10.1016/j.matdes.2009.11.053.

[12] X. Chu, L. Leotoing, D. Guines, E. Ragneau, Temperature and strain rate influence on AA5086 forming limit curves: Experimental results and discussion on the validity of the M-K model, International Journal of Mechanical Sciences 78 (2014) 27–34. doi:10.1016/j.ijmecsci.2013.11.002.

[13] L. Wang, M. Strangwood, D. Balint, J. Lin, T. Dean, Formability and failure mechanisms of AA2024 under hot forming conditions, Materials Science and Engineering: A 528 (6) (2011) 2648–2656. doi:10.1016/j.msea.2010.11.084.

[14] A. Kacem, H. Laurent, S. Thuillier, Influence of temperature on the formability of an aluminum alloy, ESAFORM 2021 (apr 2021). doi:10.25518/esaform21.1511.

[15] J. Rice, D. Tracey, On the ductile enlargement of voids in triaxial stress fields, Journal of the Mechanics and Physics of Solids 17 (3) (1969) 201–217. doi:10.1016/0022-5096(69)90033-7.

[16] M. Ayada, T. Higashino, K. Mori, Central bursting in extrusion of inhomogeneous materials, Advanced Technology of Plasticity 1 (1987) 553–558.

[17] Y. Lou, H. Huh, S. Lim, K. Pack, New ductile fracture criterion for prediction of fracture forming limit diagrams of sheet metals, International Journal of Solids and Structures 49 (25) (2012) 3605–3615. doi:10.1016/j.ijsolstr.2012.02.016.

[18] Y. Lou, H. Huh, Extension of a shear-controlled ductile fracture model considering the stress triaxiality and the Lode parameter, International Journal of Solids and Structures 50 (2) (2013) 447–455. doi:10.1016/j.ijsolstr.2012.10.007.

[19] M. Oyane, Criteria of ductile fracture strain, Bulletin of JSME 15 (90) (1972) 1507–1513. doi:10.1299/jsme1958.15.1507.

[20] Y. Ko, J. Lee, H. Huh, H. Kim, S. Park, Prediction of fracture in hub-hole expanding process using a new ductile fracture criterion, Journal of Materials Processing Technology 187-188 (2007) 358–362. doi:10.1016/j.jmatprotec.2006.11.071.

[21] Y. Bai, T. Wierzbicki, A new model of metal plasticity and fracture with pressure and Lode dependence, International Journal of Plasticity 24 (6) (2008) 1071–1096. doi:10.1016/j.ijplas.2007.09.004.

[22] Y. Bai, T. Wierzbicki, Application of extended Mohr-Coulomb criterion to ductile fracture, International Journal of Fracture 161 (1) (2010) 1–20. doi:10.1007/s10704-009-9422-8.

[23] D. Mohr, S. J. Marcadet, Micromechanically-motivated phenomenological Hosford–Coulomb model for predicting ductile fracture initiation at low stress triaxialities, International Journal of Solids and Structures 67-68 (2015) 40–55. doi:10.1016/j.ijsolstr.2015.02.024.

[24] M. Novella, A. Ghiotti, S. Bruschi, P. Bariani, Ductile damage modeling at elevated temperature applied to the cross wedge rolling of AA6082-t6 bars, Journal of Materials Processing Technology 222 (2015) 259–267. doi:10.1016/j.jmatprotec.2015.01.030.

[25] C. C. Roth, D. Mohr, Effect of strain rate on ductile fracture initiation in advanced high strength steel sheets: Experiments and modeling, International Journal of Plasticity 56 (2014) 19–44. doi:10.1016/j.ijplas.2014.01.003.

[26] G. R. Johnson, W. H. Cook, Fracture characteristics of three metals subjected to various strains, strain rates, temperatures and pressures, Engineering Fracture Mechanics 21 (1) (1985) 31–48. doi:10.1016/0013-7944(85)90052-9.

[27] J. Liu, Y. Bai, C. Xu, Evaluation of ductile fracture models in finite element simulation of metal cutting processes, Journal of Manufacturing Science and Engineering 136 (1) (nov 2013). doi:10.1115/1.4025625.

[28] R. Du, C. Mareau, Y. Ayed, E. Giraud, P. D. Santo, Experimental and numerical investigation of the mechanical behavior of the AA5383 alloy at high temperatures, Journal of Materials Processing Technology 281 (2020) 116609. doi:10.1016/j.jmatprotec.2020.116609.

[29] Q. Wang, R. Bertolini, S. Bruschi, A. Ghiotti, Anisotropic fracture behavior of AZ31 magnesium alloy sheets as a function of the stress state and temperature, International Journal of Mechanical Sciences 163 (2019) 105146. doi:10.1016/j.ijmecsci.2019.105146.

[30] J. Cao, Z. Sun, L. Huang, Z. Yin, A unified model of ductile fracture considering strain rate and temperature under the complex stress states, Journal of Materials Processing Technology 297 (2021) 117275. doi:10.1016/j.jmatprotec.2021.117275.

[31] Y. Lou, J. W. Yoon, H. Huh, Modeling of shear ductile fracture considering a changeable cut-off value for stress triaxiality, International Journal of Plasticity 54 (2014) 56–80. doi:10.1016/j.ijplas.2013.08.006.

[32] Y. Lou, H. Huh, Evaluation of ductile fracture criteria in a general three-dimensional stress state considering the stress triaxiality and the lode parameter, Acta Mechanica Solida Sinica 26 (6) (2013) 642–658. doi:10.1016/s0894-9166(14)60008-2.

[33] S. Baltic, J. Magnien, H.-P. Gänser, T. Antretter, R. Hammer, Coupled damage variable based on fracture locus: Modelling and calibration, International Journal of Plasticity 126 (2020) 102623. doi:10.1016/j.ijplas.2019.11.002.

[34] Y. Lou, L. Chen, T. Clausmeyer, A. E. Tekkaya, J. W. Yoon, Modeling of ductile fracture from shear to balanced biaxial tension for sheet metals, International Journal of Solids and Structures 112 (2017) 169–184. doi:10.1016/j.ijsolstr.2016.11.034.

[35] S. Zhang, Y. Lu, Z. Shen, C. Zhou, Y. Lou, Prediction of ductile fracture for Al6016-T4 with a ductile fracture criterion: Experiment and simulation, International Journal of Damage Mechanics (jul 2019). doi:10.1177/1056789519865771.

[36] M. Dunand, D. Mohr, Hybrid experimental–numerical analysis of basic ductile fracture experiments for sheet metals, International Journal of Solids and Structures 47 (9) (2010) 1130–1143. doi:10.1016/j.ijsolstr.2009.12.011.

[37] A. Kacem, A. Krichen, P.-Y. Manach, S. Thuillier, J.-W. Yoon, Failure prediction in the hole-flanging process of aluminium alloys, Engineering Fracture Mechanics 99 (2013) 251–265. doi:10.1016/j.engfracmech.2012.12.018.

[38] J. Li, F. Li, Y. Cui, Effect of notch radius on anisotropic fracture response of AA6061-t6 under tension process, Theoretical and Applied Fracture Mechanics 103 (2019) 102276. doi:10.1016/j.tafmec.2019.102276.

[39] Y. Lou, J. W. Yoon, H. Huh, Q. Chao, J.-H. Song, Correlation of the maximum shear stress with micro-mechanisms of ductile fracture for metals with high strength-to-weight ratio, International Journal of Mechanical Sciences 146-147 (2018) 583–601. doi:10.1016/j.ijmecsci.2018.03.025.

[40] A. Kacem, H. Laurent, S. Thuillier, Influence of experimental boundary conditions on the calibration of a ductile fracture criterion, Engineer-

ing Fracture Mechanics 248 (2021) 107686. doi:https://doi.org/10.1016/j.engfracmech.2021.107686.

[41] B. Tang, F. Wu, Q. Wang, J. Liu, N. Guo, H. Ge, Q. Wang, P. Liu, Damage prediction of hot stamped boron steel 22MnB5 with a microscopic motivated ductile fracture criterion: Experiment and simulation, International Journal of Mechanical Sciences 169 (2020) 105302–. doi:10.1016/j.ijmecsci.2019.105302.

[42] A. D. Deole, M. R. Barnett, M. Weiss, The numerical prediction of ductile fracture of martensitic steel in roll forming, International Journal of Solids and Structures 144-145 (2018) 20–31. doi:10.1016/j.ijsolstr.2018.04.011.

[43] G. Gruben, D. Morin, M. Langseth, O. Hopperstad, Strain localization and ductile fracture in advanced high-strength steel sheets, European Journal of Mechanics - A/Solids 61 (2017) 315–329. doi:10.1016/j.euromechsol.2016.09.014.

[44] GOM mbH , Aramis user manual software, 2007.

[45] H. Laurent, J. Coër, P.-Y. Manach, M.-C. Oliveira, L.-F. Menezes, Experimental and numerical studies on the warm deep drawing of an al–mg alloy, International Journal of Mechanical Sciences 93 (2015) 59–72. doi:https://doi.org/10.1016/j.ijmecsci.2015.01.009.

[46] M. C. Oliveira, L. Germain, H. Laurent, V. M. Simões, D. M. Neto, J. L. Alves, L. F. Menezes, A modified hockett-sherby law enabling the description of the thermomechanical behaviour of the AA6061-t6,

Procedia Manufacturing 47 (2020) 896–903. doi:https://doi.org/10.1016/j.promfg.2020.04.277.

[47] H. Talebi-Ghadikolaee, H. M. Naeini, M. J. Mirnia, M. A. Mirzai, H. Gorji, S. Alexandrov, Fracture analysis on U-bending of AA6061 aluminum alloy sheet using phenomenological ductile fracture criteria, Thin-Walled Structures 148 (2020) 106566. doi:10.1016/j.tws.2019.106566.

[48] Y. Lou, H. Huh, Prediction of ductile fracture for advanced high strength steel with a new criterion: Experiments and simulation, Journal of Materials Processing Technology 213 (8) (2013) 1284–1302. doi:10.1016/j.jmatprotec.2013.03.001.

[49] V. Simões, M. Oliveira, H. Laurent, L. Menezes, The punch speed influence on warm forming and springback of two al-mg-si alloys, Journal of Manufacturing Processes 38 (2019) 266–278. doi:10.1016/j.jmapro.2019.01.020.

[50] F. Bron, J. Besson, A yield function for anisotropic materials application to aluminum alloys, International Journal of Plasticity 20 (4-5) (2004) 937–963. doi:10.1016/j.ijplas.2003.06.001.

[51] F. Barlat, H. Aretz, J. Yoon, M. Karabin, J. Brem, R. Dick, Linear transfomation-based anisotropic yield functions, International Journal of Plasticity 21 (5) (2005) 1009–1039. doi:10.1016/j.ijplas.2004.06.004.

[52] S. Zhang, L. Leotoing, D. Guines, S. Thuillier, S. lai Zang, Calibration of anisotropic yield criterion with conventional tests or biaxial test, International Journal of Mechanical Sciences 85 (2014) 142–151. doi:10.1016/j.ijmecsci.2014.05.020.

[53] X. Gao, T. Zhang, M. Hayden, C. Roe, Effects of the stress state on plasticity and ductile failure of an aluminum 5083 alloy, International Journal of Plasticity 25 (12) (2009) 2366–2382. doi:10.1016/j.ijplas.2009.03.006.

[54] L.-Y. Qian, G. Fang, P. Zeng, Q. Wang, Experimental and numerical investigations into the ductile fracture during the forming of flat-rolled 5083-O aluminum alloy sheet, Journal of Materials Processing Technology 220 (2015) 264–275. doi:10.1016/j.jmatprotec.2015.01.031.

[55] D. Pantousa, T. Karavasilis, Experimental and numerical investigation of the ductile fracture of structural steel at elevated temperatures, Journal of Constructional Steel Research 177 (2021) 106444. doi:10.1016/j.jcsr.2020.106444.

[56] K. S. Pandya, C. C. Roth, D. Mohr, Strain rate and temperature dependent fracture of aluminum alloy 7075: Experiments and neural network modeling, International Journal of Plasticity 135 (2020) 102788. doi:10.1016/j.ijplas.2020.102788.

[57] N. Habibi, A. Zarei-Hanzaki, H.-R. Abedi, An investigation into the fracture mechanisms of twinning-induced-plasticity steel sheets under

various strain paths, Journal of Materials Processing Technology 224 (2015) 102–116. doi:10.1016/j.jmatprotec.2015.04.014.

Hybrid experimental-numerical approach

Ductile fracture specimens

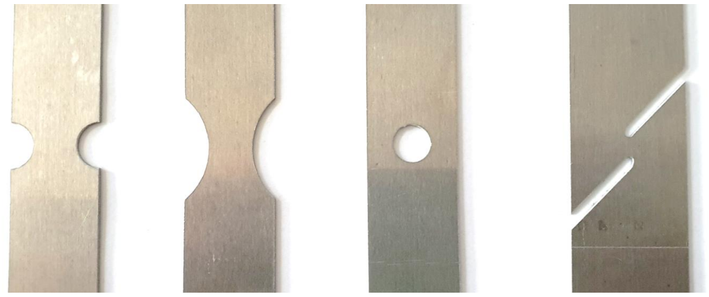

NR5 NR15 HR4 SH

FE model of fracture tests

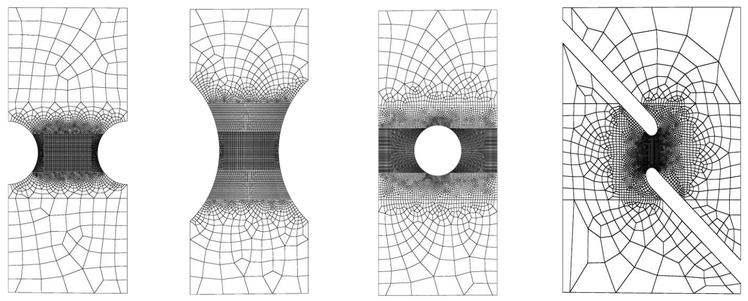

Determination of fracture strain at room and elevated temperatures

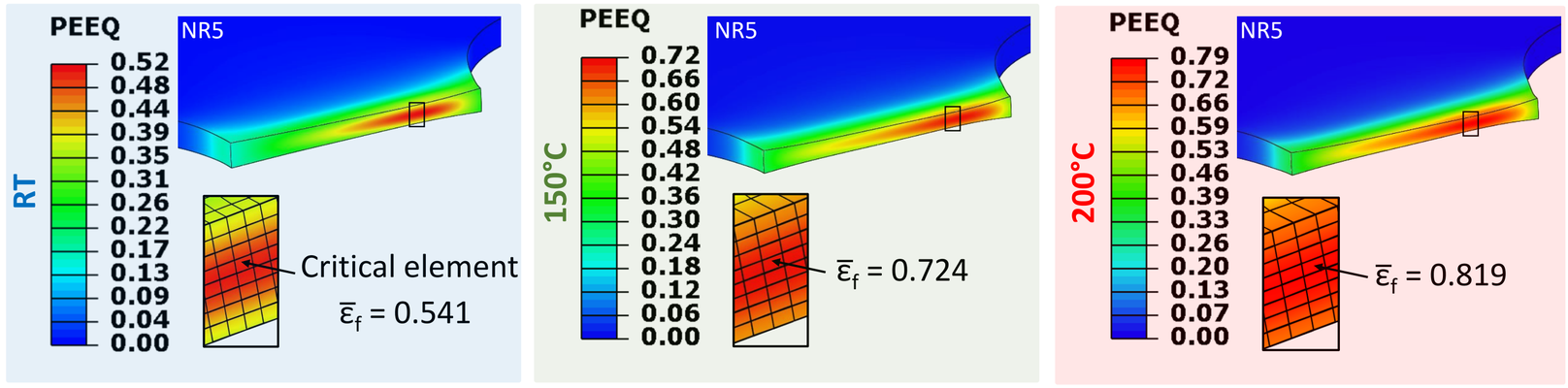

Fracture locus of AA6061-T6 at room and elevated temperatures